# Dimensional hybridity in measurement-induced criticality

Oliver Lunt,<sup>1,\*</sup> Marcin Szyniszewski,<sup>1,†</sup> and Arijeet Pal<sup>1,‡</sup>
<sup>1</sup>Department of Physics, University College London, Gower Street, London, WC1E 6BT
(Dated: December 22, 2024)

Entanglement transitions in quantum dynamics present a novel class of phase transitions in non-equilibrium systems. When a many-body quantum system undergoes hybrid quantum dynamics, consisting of unitary evolution interspersed with monitored random measurements, the steady-state can exhibit a phase transition between volume- and area-law entanglement. The role of dimension in the nature of these transitions is an open problem. There is a dimensional correspondence between measurement-induced transitions in non-unitary quantum circuits in d spatial dimensions and classical statistical mechanical models in d+1 dimensions, where the time dimension in the quantum problem is mapped to a spatial dimension in the classical model. In this work we show that the role of dimension is considerably richer by unveiling a form of 'dimensional hybridity': critical properties of the steady-state entanglement are governed by a combination of exponents consistent with d-dimensional percolation and (d+1)-dimensional percolation. We uncover this dimensional hybridity in 1+1D and 2+1D circuits using a graph-state based simulation algorithm where the entanglement structure is encoded in an underlying graph, providing access to the geometric structure of entanglement. We locate the critical point using the tripartite information, revealing area-law entanglement scaling at criticality, and showing that the entanglement transition coincides with the purification transition. The emergence of this 'dimensional hybridity' in these non-unitary quantum circuits sheds new light on the universality of measurement-induced transitions, and opens the way for analyzing the quantum error correcting properties of random unitary circuits in higher dimensions.

#### I. INTRODUCTION

Recent years have seen the exciting discovery of novel non-equilibrium phases of matter in many-body quantum systems. Quantum entanglement provides a natural framework for the taxonomy of these non-equilibrium phases. A prominent example of a non-equilibrium phase transition is the many-body localization (MBL) transition [1–6], in which the energy eigenstates switch from area-law entanglement in the MBL phase to volume-law in the chaotic phase. This singular change in the entanglement scaling means that the MBL transition is an example of an entanglement transition. MBL is also notable for the dramatic effect dimensionality is expected to have on the nature of MBL in dimensions d > 1 [7–11].

For systems without energy conservation, random unitary circuits have served as effective toy models of manybody quantum chaos [12–15]. With the advent of noisy intermediate scale quantum (NISQ) devices [16], the dynamics of pseudo-random unitary circuits can now be realized in experimental platforms, including superconducting qubits [17] and trapped ions [18]. A many-body quantum system undergoing chaotic unitary time evolution will typically thermalize, leading to volume-law entanglement in the steady state [19]. However, this thermalization and the concomitant volume law can be destroyed if the time evolution becomes non-unitary due to randomly interspersed measurements. The steady state conditioned on the measurement outcomes can then exhibit a phase

transition between volume- and area-law entanglement as a function of the measurement rate, leading to the notion of measurement-induced transitions [20–65].

These measurement-induced transitions occur in a wide variety of models, including random circuits [20–40], Hamiltonian systems [41–49], and measurement-only models [33, 50, 51, 62], and exhibit universal behavior.

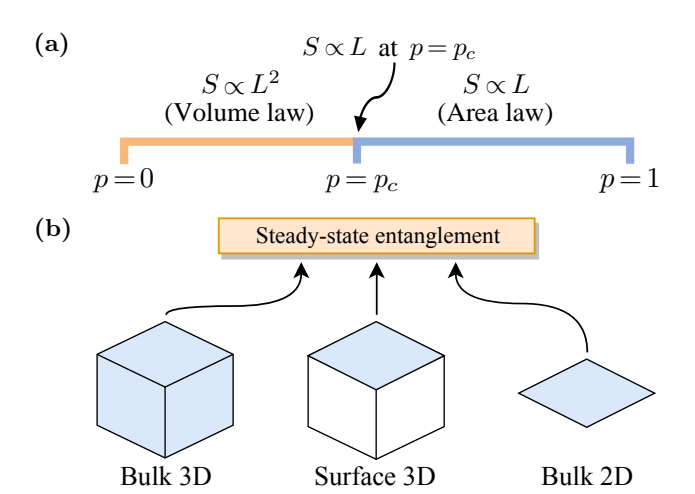


FIG. 1. (a) Phase diagram for the measurement-induced transition in 2+1D local random Clifford circuits. For measurement probabilities  $p < p_c$  the steady state exhibits volume-law entanglement, while for  $p \geq p_c$  the steady state is area-law entangled. The entanglement transition and the purification transition coincide. (b) We observe 'dimensional hybridity': in 2+1D the critical point appears to be described by exponents from both bulk 3D percolation and bulk 2D percolation, though there are some differences in surface exponents. An analogous statement holds in 1+1D hybrid quantum circuits.

<sup>\*</sup> oliver.lunt.17@ucl.ac.uk

<sup>†</sup> mszynisz@gmail.com

 $<sup>^{\</sup>ddagger}$  a.pal@ucl.ac.uk

However, the determination of the relevant universality classes has proved to be a subtle issue. In certain 1+1D systems there is a 'dimensional correspondence', where the measurement-induced transition in the 1+1D quantum system corresponds to an ordering transition in a 2+0D statistical mechanical model. Through these models, it has become clear that there is an important link between measurement-induced transitions and classical percolation, but the precise nature of this relationship is still unclear. For example, for 1+1D Haar-random circuits there are two distinct mappings to 2D percolation: one for the (n=0)-Rényi entropy (Hartley entropy) [22] which employs the minimal cut formalism [66], and another for the  $(n \ge 1)$ -Rényi entropies [29, 30] which uses the replica-trick to map the problem to 2D percolation in the limit of large local Hilbert space dimension  $q \to \infty$ .

In this work we show that the universal properties of measurement-induced transitions can be considerably richer than suggested by this 'dimensional correspondence'. In fact, we demonstrate the emergence of a form of 'dimensional hybridity'. By this we mean that this transition in (d+1)-dimensional hybrid quantum circuits has critical properties which are governed by a combination of exponents from d-dimensional percolation and (d+1)-dimensional percolation.

We provide strong support for this novel universality in both 1+1D and 2+1D hybrid Clifford circuits. Numerical simulations are performed using a graph-state based simulation algorithm (see Fig. 2) [67], which provides easy access to geometric information about the entanglement structure—the entanglement is completely fixed by the underlying graph, and we employ graph-theoretic clustering tools to analyze entanglement clusters in the steady-state (see Section V). It is through the critical properties of these entanglement clusters that we unveil the connection to d-dimensional percolation.

We complement this analysis by extending the dimensional correspondence found in 1+1D systems to higher dimensions. First, we precisely locate the critical point using the tripartite information  $I_3$  (see Section III). This allows us to unveil area-law entanglement scaling  $[S \sim \mathcal{O}(L)]$  at criticality, in constrast to 1+1D where it diverges logarithmically [22, 24]. This area-law scaling is consistent with the behavior of conformal field theories in dimensions d > 2 [68, 69]. We note that the accurate determination of the critical point using  $I_3$  was important to correctly determine the critical scaling, since even small deviations can result in scaling which looks like  $S \sim \mathcal{O}(L \log L)$  (c.f. Ref. [38] and the discussion in Appendix B).

Next we analyze the connection between this measurement-induced entanglement transition and quantum error-correction through the lens of the purification transition [27–29, 39, 58], which is characterized by a transition in the purification time of an initially maximally-mixed state—in the 'mixed phase' the state purifies in a time exponential in system size L, whereas in the 'pure phase' it purifies in a time polynomial in L. This purification transition can be viewed as a transition in the

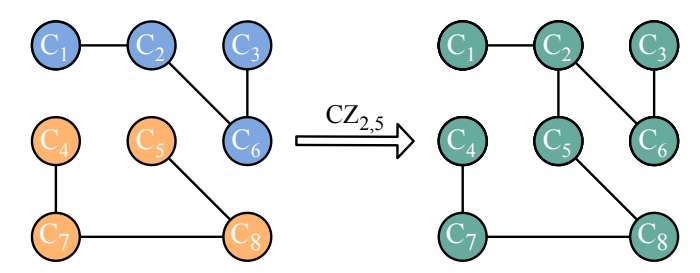


FIG. 2. We employ a graph-state based simulation algorithm [67], where the data encoding the state consists of a graph  $\mathcal G$  and a list  $\{C_i\}_{i=1}^{L^d}$  of one-qubit Cliffords. The entanglement structure is completely fixed by  $\mathcal G$ . Entanglement clusters can be found by a breadth-first search on  $\mathcal G$ , and are here highlighted in different colors. In general the action of a Clifford gate corresponds to updating  $\mathcal G$  and the list of one-qubit Cliffords. Here we illustrate the simple case of a CZ gate acting on two qubits whose one-qubit Cliffords commute with CZ; in this case the CZ gate simply toggles an edge between the qubits.

quantum channel capacity density of the hybrid quantum circuit, which governs whether the circuit can be used to generate a finite-rate quantum error-correcting code—the code rate is finite in the mixed phase, and goes to zero as one approaches the pure phase. In other words, these hybrid quantum circuits can form *emergent* quantum error-correcting codes which protect against errors given precisely by the measurements involved in the circuit.

It is not a priori obvious that these two measurementinduced transitions should coincide: the entanglement transition concerns spatial correlations in a quantum state at a fixed time, whereas the purification transition concerns correlations between quantum states at different times [28]. Their coincidence in 1+1D was explained by the fact that the 2+0D statistical mechanical model governing the purification transition is the same as that of the entanglement transition, just with different boundary conditions [29, 31]. In these models, the time coordinate of the physical circuit plays the role of imaginary time in the stat-mech model, giving an emergent symmetry between space and time [31]. In higher dimensions, however, the symmetry between space and time can be broken quite naturally. Our precise handle on the critical point allows us to demonstrate that the purification transition in 2+1D Clifford circuits continues to coincide with the entanglement transition, suggesting this phenomenon may be generic in all dimensions.

The coincidence of these two transitions then allows us to utilize the entangling and purifying dynamics of entangled ancilla qubits to extract various bulk and surface critical exponents of the transition in 2+1D Clifford circuits, and to provide evidence of conformal symmetry at the critical point (see Section IV). Most of the exponents extracted in this way are within error-bars of 3D percolation (see Table I), providing further support for the emergence of dimensional hybridity. Interestingly, we do observe small deviations from percolation in certain

Exponent	Quantum circuits		Classical percolation		
Exponent	1+1D C	2+1D C	1D P	2D P	3D P
$\nu$	1.24(7)	0.85(9)	1	4/3 = 1.333	0.877
$\eta$	0.22(1)	-0.01(5)	1	5/24 = 0.208	-0.047
$\eta_{\parallel}$	0.63(1)	0.85(4)	1	2/3 = 0.667	0.95
$\eta_{\perp}$	0.43(2)	0.46(8)	1	7/16 = 0.438	0.45
$\beta$	0.14(1)	0.40(1)	0	5/36 = 0.139	0.43
$eta_s$	0.39(2)	0.74(2)	0	4/9 = 0.444	0.85
z	1.06(4)	1.07(4)			
Entanglement clusters					
$\beta/\nu$	0.01	0.112(7)	0	5/48 = 0.104	0.49
$eta_s/ u$			0	1/3 = 0.333	0.97
$\gamma/ u$	0.9	1.65(10)	1	43/24 = 1.792	2.09
$\gamma_s/ u$			1	4/3 = 1.333	1.06
au	2.04	1.98(1)	2	187/91 = 2.055	2.19

TABLE I. Critical exponents of the measurement-induced transition in hybrid 1+1D and 2+1D random Clifford circuits, compared with those of 1D, 2D and 3D percolation (1D P, 2D P, and 3D P respectively). Exponents which appear to differ from percolation are highlighted in red. There is also evidence that the steady-state entanglement cluster distribution in d spatial dimensions has certain properties controlled by d-dimensional percolation rather than (d+1)-dimensional percolation [see Section V]. The exponents for 1+1D Clifford circuits, excluding those describing entanglement clusters, are taken from Ref. [26].

surface critical exponents (see Section IV). This is similar to the behavior observed numerically in 1+1D circuits with qubits [26, 31, 39]. One possible explanation can be found in Ref. [30], where it was found that for 1+1D circuits, although the  $q=\infty$  critical point is described by 2D percolation, at finite q a relevant operator appears which perturbs away from the percolation fixed point. The fact that numerics on qubits (q=2) nonetheless give bulk exponents close to (d+1)-dimensional percolation, but surface properties which are different, then suggests that the finite q fixed point might only be a weak perturbation from the  $q=\infty$  fixed point.

#### II. METHODS

#### A. Model

In Sections III and IV we study a 2+1D model of local random Clifford dynamics interspersed with random projective measurements. Each time step consists of a round of random 2-qubit Clifford gates with disjoint support applied to nearest-neighbors, followed by a round of projective measurements in the  $\sigma^z$  basis, where each qubit has probability p of being measured. The gates are drawn uniformly over the whole 2-qubit Clifford group. The pattern of gates applied at a given time step is determined by two indices: a 'sublattice index', which takes values in  $\mathbb{Z}_2$ , and a 'clock index', which takes values in  $\mathbb{Z}_4$ . Arranging the qubits in an  $L \times L$  square lattice with periodic boundary conditions, the sublattice index determines

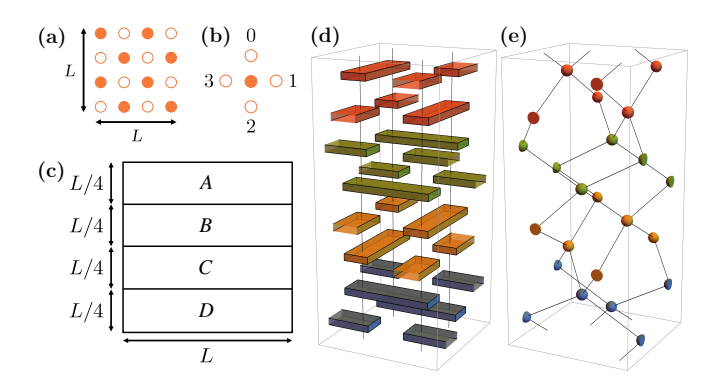


FIG. 3. (a) The sublattice index determines which sublattice of qubits, denoted by  $\bigcirc$  or  $\bigcirc$ , are used as the 'controls' for the Clifford gates in that time step. (b) Given a choice of sublattice index, the clock index determines in which direction each Clifford gate acts relative to the control. (c) The geometry used to calculate the tripartite information  $I_3(A:B:C)$ . (d) One period of the gate sequence on a  $2\times 2$  lattice with periodic boundary conditions, and time moving in the vertical direction. Different colors label different values of the clock index. (e) Unit cell of the underlying lattice structure, obtained by contracting each Clifford gate into a point.

which sublattice of qubits will act as the 'controls' for the Clifford gates (see Fig. 3a). Given a choice of sublattice, the clock index then determines which direction the Clifford gates act in relative to the control qubits. The values 0, 1, 2, and 3 correspond to gates acting up, right, down, and left from the control qubits respectively (see Fig. 3b). At the nth time step, the sublattice index has the value  $n \pmod{2}$ , and the clock index has the value  $\lfloor n/2 \rfloor \pmod{4}$ , so that the overall gate sequence has period 8 (see Fig. 3d). Since the support of the Clifford gates changes with each time step, certain quantities that depend on making a 'cut', such as the entanglement entropy of a given region, exhibit a mild periodicity related to how often the gates cross the cut. To get well-defined steady-state values, we perform a window-average over a window matching the period of the oscillations (equal to 4 time steps in this case)—all quantities in this paper have been averaged in this way.

It is worth noting that this choice of gate protocol is by no means unique. On grounds of universality, we expect the main effect of a different choice of local quantum circuit is to change the critical measurement probability  $p_c$ , with the critical exponents unaffected. One alternative was explored in Ref. [38], which used 4-local gates instead of our 2-local gates. For rank-1 measurements, they observe a critical probability of  $p_c \approx 0.54$ , which is roughly the square root of our estimated value of  $p_c \approx 0.312(2)$ . They do observe a different correlation length exponent  $\nu$ , on which we comment in Section III.

In Section V, as well as studying the 2+1D Clifford model we have just outlined, we also study a 1+1D Clifford model. This is identical to that studied in many previous works studying the 1+1D problem, and can be thought of as being controlled by a single 'sublattice index', resulting

in a 'brick-wall' structure of alternating layers of Clifford gates interspersed with random projective measurements.

#### B. Simulation method

To simulate the hybrid Clifford dynamics, we used a graph-state based algorithm [67]. This makes use of the remarkable fact that every stabilizer state can be represented as a graph state, up to the action of some 1-qubit Cliffords [70]. Simulation of stabilizer states then takes the form of updating the underlying graph structure and the list of 1-qubit Cliffords, which can be done in polynomial time.

In more detail, graph states are a class of pure quantum states whose structure is determined entirely by an underlying graph  $\mathcal{G}=(V,E)$ . Each graph vertex  $v\in V$  corresponds to a qubit, and the graph edges E determine the preparation procedure for the state. To prepare the graph state  $|\mathcal{G}\rangle$ , we start from the initial product state  $|\psi_0\rangle=[(|0\rangle+|1\rangle)/\sqrt{2}]^{\otimes N}$ , where N is the number of qubits, and then apply a CZ gate to each pair of qubits which are connected by an edge in the graph  $\mathcal{G}$ .

Stabilizer states are the states which can be prepared from the initial product state  $|0\rangle^{\otimes N}$  by acting with gates from the N-qubit Clifford group  $\mathcal{C}_N$ . The set of stabilizer states is larger than that of graph states, but not by much: all stabilizer states can be written as a graph state, up to the action of some gates from the 1-qubit Clifford group  $\mathcal{C}_1$  [which contains only 24 gates, up to phase]. Single qubit gates are then trivial to perform, taking  $\Theta(1)$  time. Two-qubit Cliffords take time  $\mathcal{O}(d^2)$ , where d is the maximum vertex degree of the qubits involved in the gate, and single-qubit Z-basis measurements take time  $\mathcal{O}(d)$ . This makes graphs with low connectivity, which can roughly be identified with low entangled states, easier to simulate.

To wit, the graph structure completely determines the entanglement of the corresponding quantum state. Given a bipartition of the system into subsystems A and B, the (Rényi or von Neumann) entanglement entropy  $S_A$  is given by

$$S_A = \operatorname{rank}(\Gamma_{AB}),$$
 (1)

where  $\Gamma_{AB}$  is the submatrix of the adjacency matrix characterizing edges between subsystems A and B [70]. We note that for stabilizer states all Rényi entropies (including the von Neumann entropy) are equal [71].

To simulate an initially mixed state  $\rho$ , we introduce an auxiliary system to obtain a purification of  $\rho$ . We then perform time-evolution on the resultant pure state, with the quantum circuit acting as the identity on the purifying system. For the maximally-mixed initial state on N qubits,  $\rho = 1/2^N$ , this corresponds to the pure state simulation of N Bell pairs, where the system dynamics acts only on one half of the Bell pairs. This purification simulation method does mean that N-qubit mixed states are harder to simulate than N-qubit pure states, but not

as hard as 2N-qubit pure states, since the purifying qubits typically have a lower vertex degree than the original qubits.

#### C. Transition diagnostics

As well as the entanglement entropy  $S_A$ , we also study the tripartite mutual information

$$I_3(A:B:C) = I_2(A:B) + I_2(A:C) - I_2(A:BC), (2)$$

where  $I_2(A:B) = S_A + S_B - S_{AB}$  is the mutual information. It is easy to see that for pure states, given a partition of the system into 4 subsystems, the tripartite information of 3 of the subsystems does not depend on the choice of subsystems, so from now on we will simply write  $I_3 \equiv I_3(A:B:C)$ . We calculate  $I_3$  for the partition shown in Fig. 3c. Notice that a vertical slice of this geometry gives a circle divided into four equal sections. In 1+1D this partitioning was successfully employed to study the entanglement transition because, at least within the minimal cut picture [66], it cancels out any boundary terms corresponding to the entanglement cost of a domain wall traversing from the circuit boundary to the percolating cluster in the bulk of the circuit [26, 28]. This then suggests that in 1+1D,  $I_3$  is extensive in the volumelaw phase,  $\mathcal{O}(1)$  at criticality, and zero in the area-law phase. In 2+1D, we argue that, for this particular choice of geometry,  $I_3$  remains  $\mathcal{O}(1)$  at criticality, with its overall behavior described by

$$I_3(p,L) = \begin{cases} \mathcal{O}(L^2), & p < p_c \\ \mathcal{O}(1), & p = p_c \\ 0, & p > p_c \end{cases}$$
 (3)

This implies that the values of  $I_3(p, L)$  should coincide for different system sizes at  $p = p_c$ , allowing for reliable location of the critical point. We further discuss our choice of geometry for  $I_3$  in Appendix B.

### III. ENTANGLEMENT TRANSITION

To accurately estimate the location of the critical point, it is necessary to determine the correct scaling of  $I_3$ . To that end, we must rule out plausible scalings which are different from the one proposed in Eq. (3). We have also investigated the possibility that  $I_3 \propto L$  at the critical point, which would suggest that the values of  $I_3(p,L)/L$  should coincide at  $p=p_c$ . We detail evidence against this scaling form in Appendix A.

The steady-state values of  $I_3(p,L)$  are plotted in Fig. 4. Given the scaling in Eq. (3), the curves should coincide at the critical point. To determine the critical point and the correlation length exponent  $\nu$  we make the finite-size scaling ansatz

$$I_3(p,L) \sim F[(p-p_c)L^{1/\nu}],$$
 (4)

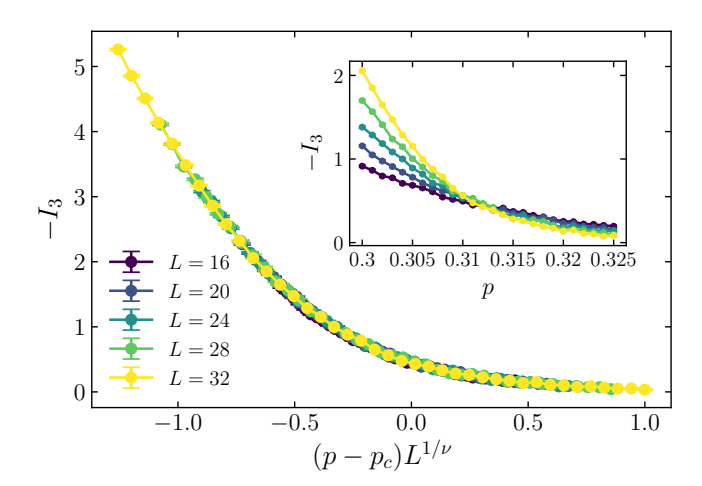


FIG. 4. The steady-state  $I_3$  as a function of  $(p-p_c)L^{1/\nu}$ , where  $p_c \approx 0.312(2)$  and  $\nu \approx 0.85(9)$ . The inset shows the uncollapsed data. This dataset consists of  $5 \times 10^4$  circuit realizations.

where  $F[\cdot]$  is a single-parameter scaling function. We determine the optimal parameters by minimizing a cost function  $\epsilon(p_c, \nu)$  which measures deviations of a point from a linear interpolation between its neighbors [26, 72 (see Appendix B for details). The resulting data collapse is of excellent quality, with  $p_c \approx 0.312(2)$  and  $\nu \approx 0.85(9)$ , where the error bars correspond to the range of values for which the cost function is less than 2 times its minimum value. We note that this value of  $\nu$  is reasonably close to the 3D percolation value of  $\nu_{\rm perc} \approx 0.877$  [73], suggesting that the close relationship between exponents of the entanglement transition and percolation, even at low local Hilbert space dimension, continues to hold in 2+1D. We also note that our value of  $\nu$  is significantly larger than that reported in Ref. [38]  $(\nu \approx 0.67)$ ; we attribute this to the fact that we extract  $\nu$ by a data collapse not of the half-plane entanglement but of the tripartite information, which coincides for different system sizes at the critical point and so provides a much more accurate estimator of the critical point. A similar scenario occurs in 1+1D [26]. We discuss this further in Appendix B.

Let us briefly comment on the value of  $p_c \approx 0.312$  obtained for the critical measurement probability. This value coincides with the threshold for site percolation on the simple cubic lattice [74], but as far as we are aware this is a coincidence; in fact our gate model maps to the lattice shown in Fig. 3e, which exhibits a bond percolation transition at  $p_c = 0.3759(2)$ . We expect other gate models to give different values of  $p_c$  (see Ref. [38]) but the same critical exponents. It is also interesting to compare our value of  $p_c$  to the upper bound derived in Ref. [27], which modeled the volume-law phase as forming a dynamically-generated non-degenerate quantum error-correcting code, allowing them to apply the quantum Hamming bound. The bound on  $p_c$  depends only on the local Hilbert space dimension q (not on the spatial

dimension), and for q=2 gives  $p_c\lesssim 0.1893$ . While this bound was satisfied by 1+1D Haar-random and Clifford circuits ( $p_c\approx 0.17$  [26]), here we see that it is strongly violated in 2+1D Clifford circuits. A similar violation has also been observed in all-to-all models [28], where it was pointed out that if these hybrid dynamics which violate this upper bound are to generate quantum error-correcting codes, these codes must be degenerate. Finally, we note that the value of  $I_3$  at criticality,  $I_3^{2+1D}(p_c)=-0.47(8)$ , is within error-bars of the value for 1+1D Clifford circuits,  $I_3^{1+1D}(p_c)=-0.56(9)$  [26], suggesting the possibility that at criticality  $I_3$  could reach an  $\mathcal{O}(1)$  constant which is independent of dimension.

Having established the location of the critical point via finite-size scaling of  $I_3$ , we study the scaling properties of the entanglement entropy in the different phases. We propose the following scaling for the 2+1D circuit:

$$S(p,L) \sim \begin{cases} L(1 - \frac{c}{\xi}) + A\frac{L^2}{\xi^2}, & p < p_c, \\ L, & p = p_c, \\ L(1 - \frac{c}{\xi}), & p > p_c, \end{cases}$$
 (5)

where  $\xi = |p - p_c|^{-\nu}$  is the correlation length and c, A are unknown constants. Such scaling implies the data collapse of the entropy is possible using a similar ansatz as in the 1+1D circuit [22, 24],

$$S(p, L) - S(p_c, L) = F[(p - p_c)L^{1/\nu}],$$
 (6)

where  $F[\cdot]$  is a single-parameter scaling function, depending only on  $L/\xi$ .

In order to see the origin of this proposed scaling form, we draw from the similarity to the 1+1D case, where the behavior of entropy can be intuitively understood by considering the Hartley entropy  $S_0$ . For Haar random circuits  $S_0$  can be mapped exactly to classical percolation in 2D [22]: each projective measurement cuts a bond of the underlying lattice and prevents percolation; Hartley entropy of a region is then calculated as the minimal number of cuts needed to separate said region at the final-time boundary from the rest of the circuit. This mapping extends naturally to d+1D circuits, where  $S_0$  corresponds to a minimal-cut d-dimensional membrane. Near criticality, the 'nodes-and-links' picture of percolation [75, 76] gives an insight into the scaling properties of  $S_0$  (see Fig. 5) and shows two important contributions: from the bulk, and from the edge.

For  $p < p_c$ , percolation in the bulk of the circuit is possible due to unbroken bonds forming a 'wire frame' consisting of dense clusters of bonds (nodes) connected by long chains of unbroken bonds (links). Each cell in the frame is of the size of the correlation length  $\xi$  and, if traversed by the minimal-cut membrane, gives a contribution of O(1) to the entropy [see Fig. 5(a) and (c) for 2D and 3D examples]. Counting the number of cells results in the bulk of the circuit contributing  $\sim (L/\xi)^d$  to  $S_0$ , the source of the volume-law scaling.

The second relevant contribution comes from the finaltime boundary of the circuit [see Fig. 5(b)]. This edge

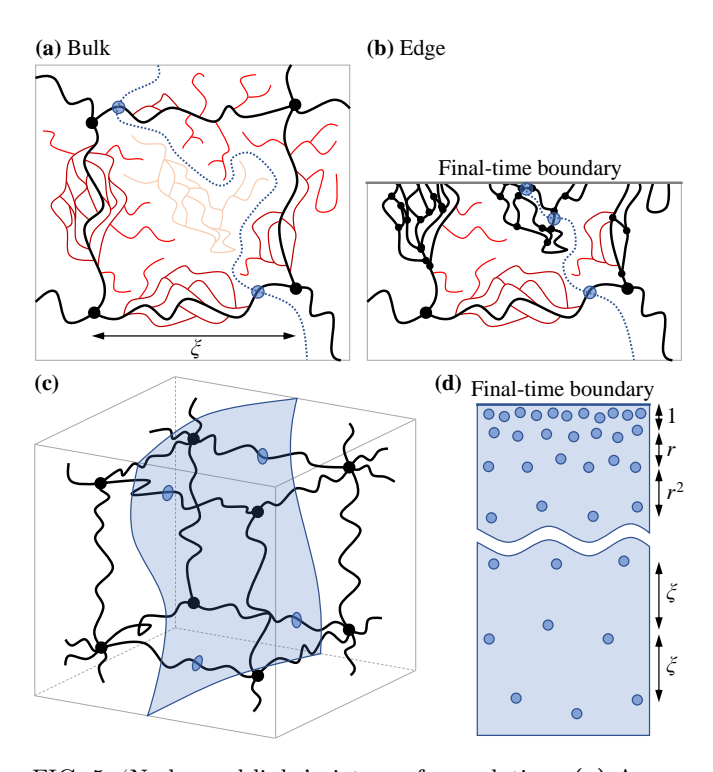


FIG. 5. 'Nodes and links' picture of percolation. (a) An example of percolation in the bulk of a 2D system. Percolating bonds cluster within nodes (black dots) connected by links (thick black lines), forming a 'wire frame'. Average distance between nodes is the correlation length  $\xi$ . There are also smaller structures on the links (dark red), dead ends (red) and structures unconnected to the frame (orange). Minimal-cut path (blue dotted line) can be deformed to only cut through the links (cuts indicated by transparent blue circles), causing an O(1) contribution to the entropy. (b) The same example, but in the presence of the final-time boundary. Every structure touching the edge is promoted to be part of the frame. Minimal-cut path generically starts within a smaller structure of size O(1), having now to traverse through larger and larger chambers in order to reach structures of size  $\xi$ . (c) Percolation in the bulk of a 3D system (showing only nodes and links for simplicity). Minimal-cut membrane can be deformed, contributing O(1) to the entropy per one cell of the frame. (d) Flattened minimal-cut membrane, showing all the necessary cuts. Near the edge, the membrane traverses layers of structures of increasingly larger sizes (with approximate common ratio r).

cuts through not only the links and nodes discussed above, but also through smaller structures, dead ends, and other structures normally unconnected to the main mesh. This results in the minimal-cut membrane having to generically cut through a large number of small mesh cells right next to the boundary, then through layers of consecutively larger cells, until the cell size reaches  $\xi$  [see Fig. 5(d)]. Assuming a geometric progression of cell sizes with common ratio r>1 [22], the number of cells in the ith layer is  $\sim (L/r^i)^{d-1}$ , while the total number of layers is  $\sim \log_r \xi$ . We then arrive at an important result: the total contribution from the boundary for 1+1D is  $\sim \log \xi$ ,

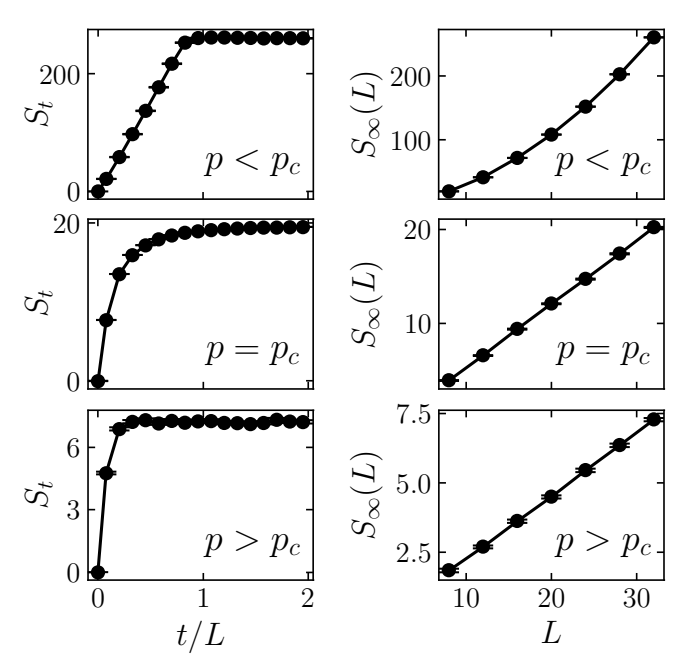


FIG. 6. Dynamics and steady-state behavior of the half-plane entanglement  $S(L/2 \times L)$  in the volume-law  $(p < p_c)$ , critical  $(p = p_c)$ , and area-law  $(p > p_c)$  phases. The left column shows the dynamics for L = 32, with  $S_t \propto t$  for  $p < p_c$ ,  $S_t \propto \log t$  for  $p = p_c$ , and  $S_t$  saturating in  $\mathcal{O}(1)$  time for  $p > p_c$ . The right column shows the steady-state scaling, with  $S_{\infty}(L) \sim \mathcal{O}(L^2)$  for  $p < p_c$ , and  $S_{\infty}(L) \sim \mathcal{O}(L)$  for  $p \geq p_c$ . We use p = 0.1, p = 0.312, and p = 0.4 for the volume-law, critical, and area-law plots respectively.

while for higher dimensions is  $\sim (1-c/\xi^{d-1})L^{d-1}$ . This term is in general responsible for the area-law scaling, but at the critical point  $p=p_c$  (when  $\xi \to L$ ) it results in logarithmic scaling in 1+1D, and area-law scaling in higher dimensions.

Fig. 6 presents our results for the entanglement entropy, showing an excellent agreement with the scaling ansatz in Eq. (5). Notably, we observe area-law scaling at the critical point (consistent with the recent results of Ref. [62]), possibly with subleading additive logarithmic corrections, but not with multiplicative logarithmic corrections ( $L \log L$ ), as implied in Ref. [38]. We note however that if one assumes a lower transition point ( $p \approx 0.29$ ), numerics may seem like a  $L \log L$  behavior for small system sizes, suggesting that correctly locating the critical value  $p_c$  is crucial to making any statements on scaling of entropy at criticality. As explained above, data collapse of  $I_3$  pinpoints the precise value of  $p_c$ , allowing us to determine the correct critical scaling behavior.

Moreover, at these system sizes we cannot directly observe the presence of a subleading additive  $\log L$  term, but we also cannot rule it out since it may have a small coefficient. Such a subleading additive  $\log L$  is predicted by a calculation from capillary wave theory [55, 77] which evaluates the free energy cost of inserting an Ising domain wall membrane in the quantum circuit's spacetime bulk,

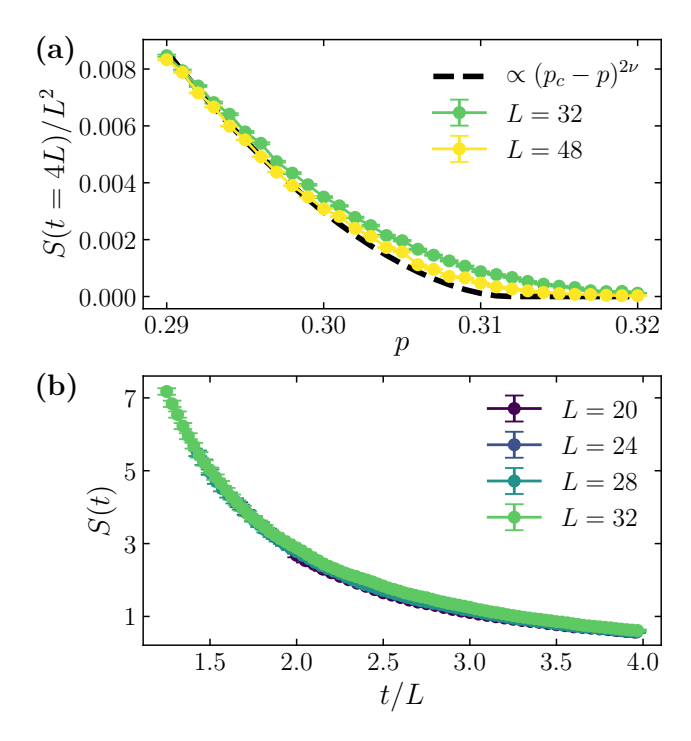


FIG. 7. (a) The entropy density of an initially maximally-mixed state after evolving for a time t=4L. The black dashed line shows the function  $A(p_c-p)^{2\nu}$  with  $A\approx 11.7$ , and  $p_c$  and  $\nu$  determined from finite-size scaling of  $I_3$ . At these system sizes there is still some finite-size drift in the data, but it seems to be approaching the curve described by  $A(p_c-p)^{2\nu}$ . (b) Purification dynamics at  $p=p_c$ . The data collapse onto a single curve when plotted in terms of t/L, indicating a dynamical critical exponent of  $z\approx 1$  [the optimal fitted value is z=1.07(4)]. Non-universal early-time dynamics are excluded from the fit.

with the boundary condition that at the boundary of the circuit corresponding to the final time the membrane is pinned to the region for which one wants to calculate the entanglement entropy. The subleading  $\log L$  then corresponds to an entropic contribution to the free energy from 'thermal' fluctuations of the membrane at finite 'temperature' (here corresponding to nonzero measurement probability). In general, the appearance at criticality of an area-law with additive log corrections is reminiscent of the behavior of higher-dimensional conformal field theories [68, 69]. There is also the possibility of a sublinear power-law correction, analogous to the  $\sim L^{0.38}$  correction observed numerically in 1+1D Clifford circuits [55], which could indicate a more complex entanglement domain wall structure than the simple Ising structure that predicts the logarithmic correction.

## IV. PURIFICATION TRANSITION

In this section, we investigate the purification transition and demonstrate that it coincides with the entanglement transition studied in Section III. To do so we study the

entanglement entropy density  $S/L^2$  of a maximally-mixed initial state after being time-evolved for time t = 4L. In the 'pure phase', the state purifies in time linear in system size L, implying  $S/L^2 \to 0$  for  $t \propto L$  but sufficiently large (t = 4L suffices), while in the 'mixed phase' the purification time is exponential in L, so that after the time t = 4L we expect the entropy density to remain finite. Fig. 7 shows the entanglement entropy density as a function of measurement probability p. The entropy density vanishes close to the critical point  $p_c \approx 0.312$  of the entanglement transition. For these system sizes, there still exists some appreciable finite-size drift, but it appears to be such that the entropy density vanishes increasingly close to  $p_c \approx 0.312$  as the system size increases. The black dashed curve shows the function  $A(p_c - p)^{2\nu}$ , with A a constant and  $p_c$  and  $\nu$  fixed from the entanglement transition. The exponent  $2\nu$  is motivated by the scaling of the entanglement entropy in Eq. (5), where the  $\mathcal{O}(L^2)$ term controlling the entropy density appears with the coefficient  $\xi^{-2} \sim (p_c - p)^{2\nu}$ . The convergence of the entropy density to the scaling form  $A(p_c - p)^{2\nu}$  therefore provides strong evidence that the purification transition indeed coincides with the entanglement transition and that the estimation of  $\nu$  in the previous section is correct.

Having established the coincidence of these two transitions, we now extract further critical exponents of the transition using the local order parameter proposed in Ref. [39] of the entanglement entropy of an ancilla qubit entangled with the system but not directly acted on by the circuit dynamics. First, we extract the anomalous scaling exponents  $\eta$ ,  $\eta_{\parallel}$ , and  $\eta_{\perp}$  controlling the power-law decay of bulk-bulk, surface-surface, and surface-bulk twopoint correlation functions at criticality. In percolation, these quantities control the probabilities that two distant sites, living either in the bulk or on the surface, belong to the same cluster. To determine these exponents we study the dynamics at  $p = p_c$  of the mutual information between two ancilla qubits separated by a distance L/2 [26], which provides an upper bound on connected correlation functions [78]. The ancilla qubits are entangled with the system at a time  $t_0$ . We use different values of  $t_0$  and different boundary conditions to extract the different exponents:  $\{t_0 = 2L, \text{ periodic}\}\$  for  $\eta$ ,  $\{t_0 = 0, \text{ periodic}\}\$  for  $\eta_{\parallel}$ , and  $\{t_0 = 2L, \text{ open}\}\$  for  $\eta_{\perp}$ . Conformal symmetry z=1 at the critical point (see Fig. 7b) implies that in D spacetime dimensions the mutual information between two qubits separated by a distance r should assume the scaling form

$$I_2(t,r) \sim \frac{1}{r^{D-2+\eta}} G\left[\frac{t-t_0}{r}\right],$$
 (7)

where  $G[\cdot]$  is a single-parameter scaling function, and the exponent depends on the choice of  $t_0$  and boundary conditions, as outlined above. Thus in this 2+1D spacetime circuit, we can extract the exponents by performing data collapses of  $L^{1+\eta}I_2[(t-t_0)/L, L/2]$ , as shown in Fig. 8. For the bulk-bulk exponent  $\eta$  and the surface-bulk exponent  $\eta_{\perp}$ , we obtain the values  $\eta \approx -0.01(5)$ 

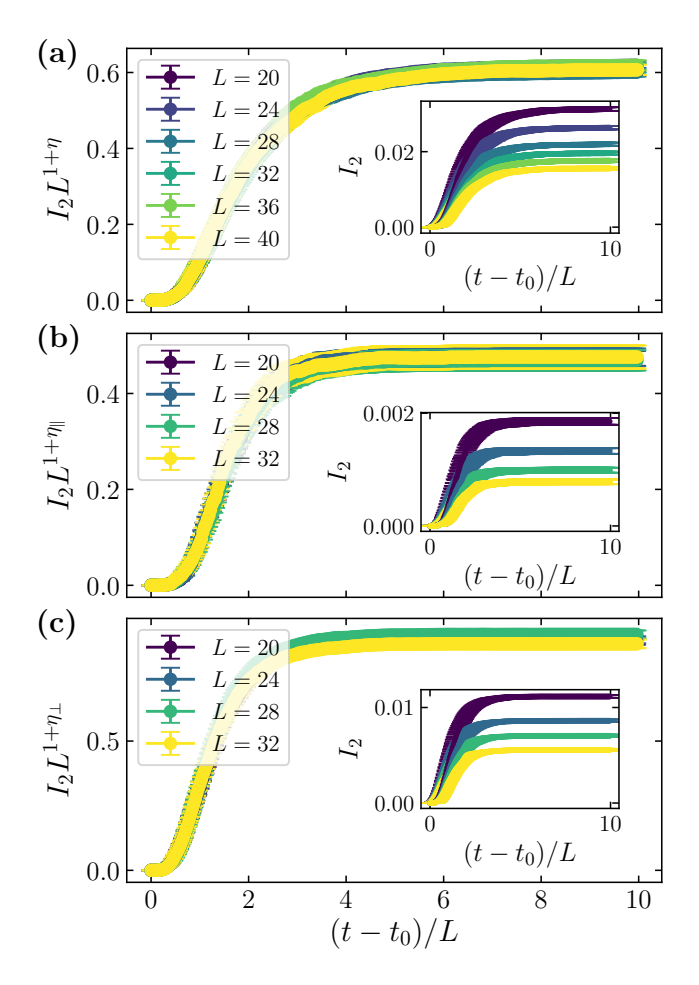


FIG. 8. Extraction of the anomalous scaling exponents  $\eta \approx -0.01(5)$ ,  $\eta_{\parallel} \approx 0.85(4)$ , and  $\eta_{\perp} \approx 0.46(8)$ , shown in (a), (b), and (c) respectively, via data collapse at  $p=p_c$  of the mutual information  $I_2$  between two ancilla qubits which are entangled at time  $t_0$  with two system qubits a distance L/2 apart. The different exponents are extracted using different boundary conditions and different values of  $t_0$  [see main text]. The insets show the uncollapsed data. The  $\eta$  dataset consists of  $2.5 \times 10^5$  circuit realizations, while the  $\eta_{\parallel}$  and  $\eta_{\perp}$  datasets each consist of  $10^6$  circuit realizations.

and  $\eta_{\perp} \approx 0.46(8)$ , which are within error-bars of the 3D percolation values  $\eta_{\rm perc} = -0.047$  and  $\eta_{\perp,\rm perc} = 0.45$  [79]. However, for the surface-surface exponent  $\eta_{\parallel}$ , we obtain the value  $\eta_{\parallel} \approx 0.85(4)$ . This is not within error-bars of the 3D percolation value  $\eta_{\parallel, \text{perc}} = 0.95$ , indicating a possible difference in surface behavior. The error-bars on our exponent estimates capture only the statistical error, so it is possible that there are still significant finite-size corrections. However, we note that a similar deviation in  $\eta_{\parallel}$  (and in  $\eta_{\perp}$ ), was observed in 1+1D Haar-random circuits (though not in Clifford circuits) [26]. In this case, a deviation only in  $\eta_{\parallel}$  would not be consistent with the scaling relation  $2\eta_{\perp} = \eta + \eta_{\parallel}$ , but the error-bars on our estimates are large enough that there could also be small deviations in  $\eta_{\perp}$  that provide the necessary contribution to restore the scaling relation.

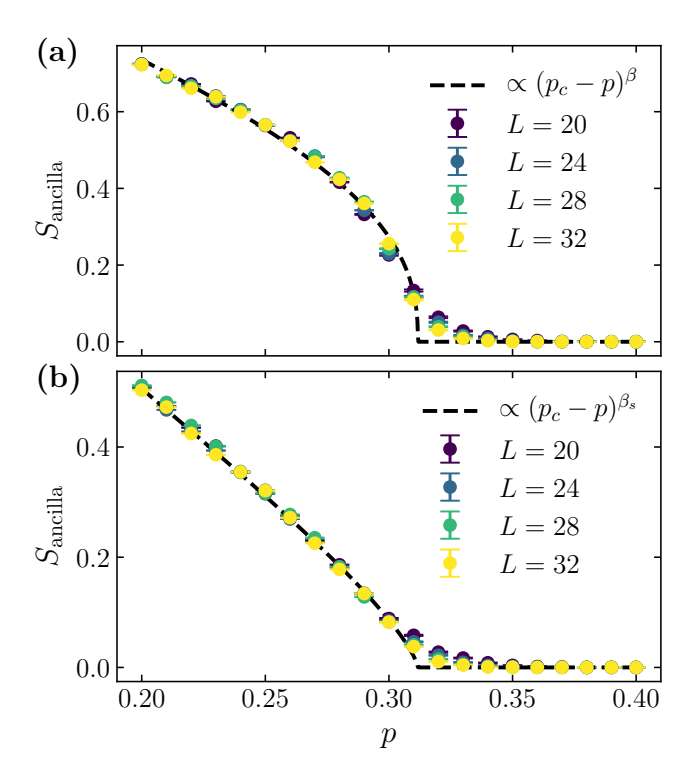


FIG. 9. Extracting the exponents  $\beta$  and  $\beta_s$  using the entropy  $S_{\rm ancilla}$  of an ancilla qubit which is maximally entangled with a bulk qubit at a time  $t_0$ , and then further evolved for a time t=2L. (a) The bulk exponent  $\beta$  is extracted using  $t_0=2L$ . The black dashed curve shows the function  $B(p_c-p)^{\beta}$  where  $B\approx 3.2$  and  $\beta\approx 0.40(1)$ . (b) The surface exponent  $\beta_s$  is extracted using  $t_0=0$ . There the black dashed curve shows the function  $C(p_c-p)^{\beta_s}$  where  $C\approx 4.6$  and  $\beta_s\approx 0.74(2)$ . In both cases,  $p_c\approx 0.312$  is fixed by finite-size scaling of  $I_3$ . This dataset consists of  $10^4$  circuit realizations.

Next, we extract the exponents  $\beta$  and  $\beta_s$  controlling the behavior of the order parameter as a function of p. In percolation,  $\beta$  controls the probability  $P(p) \sim |p - p_c|^{\beta}$ that a site in the bulk will belong to the infinite percolating cluster, while  $\beta_s$  does the same but for a site on the surface. To extract these exponents we study the entanglement entropy of an ancilla qubit, entangled with the system at time  $t_0 = 2L$  for  $\beta$  and time  $t_0 = 0$  for  $\beta_s$ , and subsequently time-evolved for a further time t = 2L. Fig. 9 shows the ancilla entropy  $S_{\text{ancilla}}$  as a function of measurement probability p for the cases relevant to  $\beta$  and  $\beta_s$ . For the bulk exponent  $\beta$ , the data are well described by the function  $B(p-p_c)^{\beta}$  with B a constant,  $p_c \approx 0.312$ fixed by the entanglement transition, and  $\beta \approx 0.40(1)$ . This is close to the 3D percolation value of  $\beta_{\rm perc} \approx 0.43$ . However, for the surface exponent  $\beta_s$ , the data are well described by the function  $C(p_c-p)^{\beta_s}$ , where  $\beta_s \approx 0.74(2)$ . This is somewhat different from the 3D percolation value of  $\beta_{s,perc} \approx 0.85$ . The value of  $\beta_s$  is quite sensitive to the value of  $p_c$ ; we estimate that to obtain  $\beta_s \approx 0.85$ one would have to have  $p_c \approx 0.318$ , which does not seem tenable given the clear crossing point in  $I_3$  (see inset of Fig. 4). There are also some small deviations from

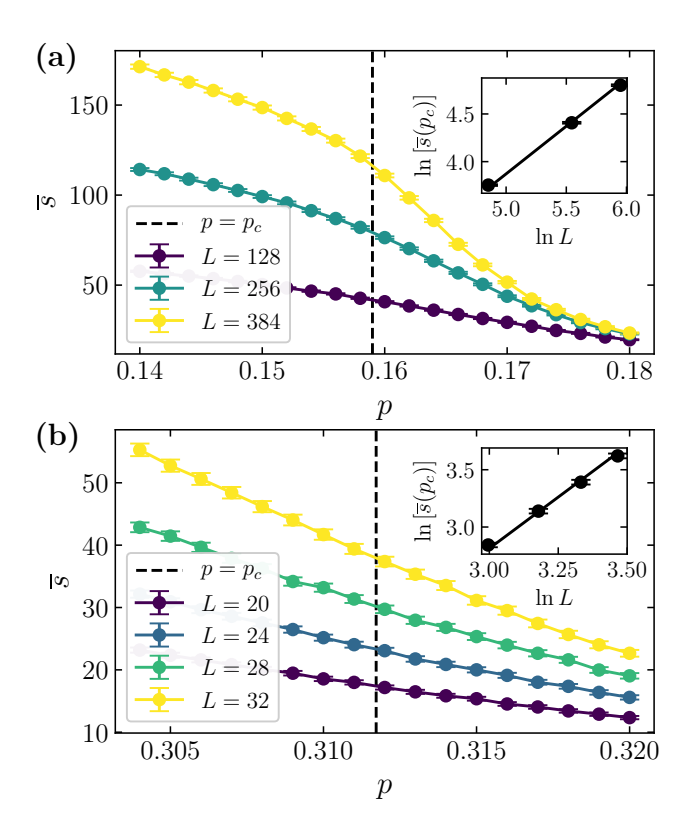


FIG. 10. The average size  $\bar{s}$  of all entanglement clusters in the steady-state for (a) 1+1D and (b) 2+1D Clifford circuits. The insets show log-log plots of this quantity at  $p=p_c$ , with the behaviour well described by the power law  $\bar{s}\sim L^{\gamma/\nu}$ , where  $\gamma/\nu=1$  and  $\gamma/\nu=43/24$  are given by the exponents from one- and two-dimensional bulk percolation respectively (shown as the solid black lines).

the scaling around  $p \approx p_c$ , but these seem to decrease with system size. We therefore tentatively conclude that the surface critical exponent  $\beta_s$  may also differ from 3D percolation. The fact that we observe both the surface exponents  $\beta_s$  and  $\eta_{\parallel}$  to be smaller than the corresponding values from percolation is consistent with the scaling relation  $2\beta_s = \nu(D-2+\eta_{\parallel})$ , where D=3 is the number of spacetime dimensions.

#### V. ENTANGLEMENT CLUSTERS

Finally, with the aim of further exploring connections with percolation, we investigate entanglement clusters in the steady state. Working within the graph-state framework for simulating stabilizer states, we define an entanglement cluster in the graph-theoretic sense: two spins are in the same cluster if there is a connected path between them (see Fig. 2 for an example). We will mainly study the size s of the clusters, defined for a given cluster as the number of spins it contains. This is clearly quite a coarse-grained notion of entanglement, since different spins in the same cluster can be entangled by different amounts. Nonetheless, it provides some insight into how

multipartite is the steady-state entanglement.

We note that this is inherently a different percolation problem to that considered in Ref. [22] to control the Hartley entropy, which involved percolation on the bonds in the (d+1)-dimensional spacetime circuit which were unbroken by measurements. The problem here is instead within a single time slice, and edges correspond not to connections between unitary gates, but to a degree of entanglement between the connected spins. It is worth noting that these entanglement graphs are potentially highly non-local, especially in the volume law phase, owing to the presence of long-range entanglement. We will see that certain quantities in the steady-state of the (d+1)dimensional quantum circuit appear to be controlled by exponents close to those of bulk d-dimensional percolation. This is surprising in several senses. First, that it differs from the (d+1)-dimensional percolation that seems to describe several aspects of the measurement-induced transition studied in previous sections. In a sense this means that we are seeing much more connectivity than would be expected on the surface of (d+1)-dimensional percolation. Second, that the universality class corresponds to a low-dimensional model, given the potentially high dimension of the entanglement graph in the presence of non-local entanglement—we discuss the effective dimensionality of the entanglement graph further in Appendix C. Finally, that we observe d-dimensional percolation exponents even when d=1, where there is quite a different role for randomness in the percolation critical point compared to the quantum circuit critical point—after all, for 1D percolation the critical probability is  $p_c = 1$  (i.e. zero randomness), whereas in the hybrid quantum circuit  $1 - p_c \approx 0.84$  (i.e. nonzero randomness).

To find the entanglement clusters, we employ a breadthfirst search on the graph storing the steady state [80]. Fig. 10 shows the behavior of the average cluster size  $\overline{s}=\sum_s n_s s^2/\sum_{s'} n_{s'} s'$ , where the cluster number  $n_s$  is the number of clusters of size s normalized by the system volume  $L^d$ . Note that this quantity measures the average cluster size if sites are randomly selected with equal probability—if instead *clusters* are randomly selected with equal probability then the corresponding average is  $\sum_{s} n_{s} s / \sum_{s'} n_{s'}$ . At  $p = p_c$  the average cluster size should be described by the power-law  $\bar{s} \sim L^{\gamma/\nu}$ . The inset to Fig. 10a shows a log-log plot of this quantity for 1+1D Clifford circuits, with a fitted exponent of  $\gamma/\nu \approx 0.9$ . close to the value of  $\gamma/\nu = 1$  for 1D percolation [76] shown by the solid black line, and far from the values of  $\gamma/\nu = 43/24 \approx 1.79$  for bulk 2D percolation and  $\gamma_s/\nu = 4/3 \approx 1.33$  for surface 2D percolation [76]. The analogous plot for 2+1D Clifford circuits is shown in the inset to Fig. 10b, where the fitted exponent  $\gamma/\nu \approx 1.7(1)$  is close to the value  $\gamma/\nu \approx 1.79$  for bulk 2D percolation, and far from the values of  $\gamma/\nu \approx 2.09$  for bulk 3D percolation and  $\gamma_s/\nu \approx 1.06$  for surface 3D percolation [79]. Thus there seems to be a sense in which certain aspects of the steady-state entanglement are described not by bulk or surface (d+1)-dimensional percolation, but by bulk

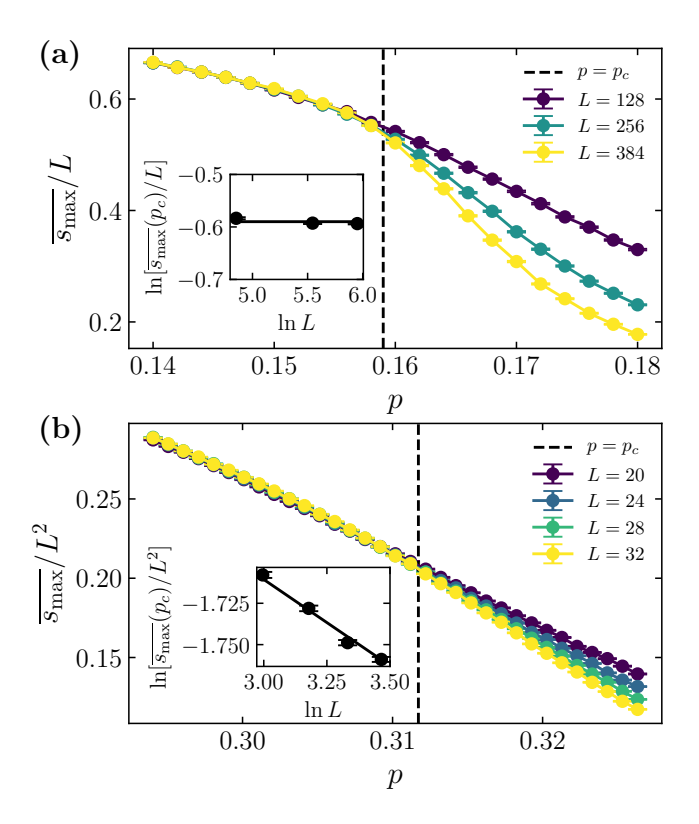


FIG. 11. The average size  $\overline{s_{\max}}$  of the largest entanglement cluster in the steady state for (a) 1+1D and (b) 2+1D Clifford circuits. The insets show log-log plots of this quantity at  $p=p_c$ , with the behavior well described by the power law  $\overline{s_{\max}}(p_c)/L^d \sim L^{-\beta/\nu}$ , where  $\beta/\nu=0$  and  $\beta/\nu=5/48$  are given by the exponents from *one*- and *two*-dimensional percolation respectively (indicated by the solid black lines).

## d-dimensional percolation.

To explore this theme further, Fig. 11 shows the average over circuit realizations of the size  $s_{\rm max}$  of the largest steady-state cluster in each realization, as a fraction of system size. This is a measure of the fractal dimension  $d_f$  of the infinite cluster since by definition  $s_{\text{max}} \sim L^{d_f} \sim L^{d-\beta/\nu}$ . The inset to Fig. 11b shows a log-log plot of  $\overline{s_{\text{max}}}(p_c)/L^d \sim L^{-\beta/\nu}$  for 2+1D Clifford circuits, which is well described by the fitted exponent  $\beta/\nu \approx 0.11(1)$ . This is close to the value  $\beta/\nu = 5/48 \approx 0.10$  from 2D percolation [76], and significantly different from the corresponding exponents from both bulk 3D percolation, where  $\beta/\nu \approx 0.49$  [73, 79], and surface 3D percolation, where  $\beta_s/\nu \approx 0.97$  [81]. The corresponding situation in 1+1D, as shown in the inset to Fig. 11a, is a little less clear-cut, since for 1D percolation we have the exponent  $\beta = 0$ , and it is hard to tell numerically if an exponent is exactly zero or simply very small. Fitting the data gives the exponent  $\beta/\nu \approx 0.01$ , which is certainly much closer to the 1D percolation exponent  $\beta/\nu = 0$  than either the bulk 2D percolation exponent  $\beta/\nu = 5/48 \approx 0.10$  [76] or the surface 2D percolation exponent  $\beta_s/\nu = 1/3 \approx 0.33$  [82], so we would argue that this scaling is consistent with the emergence of bulk

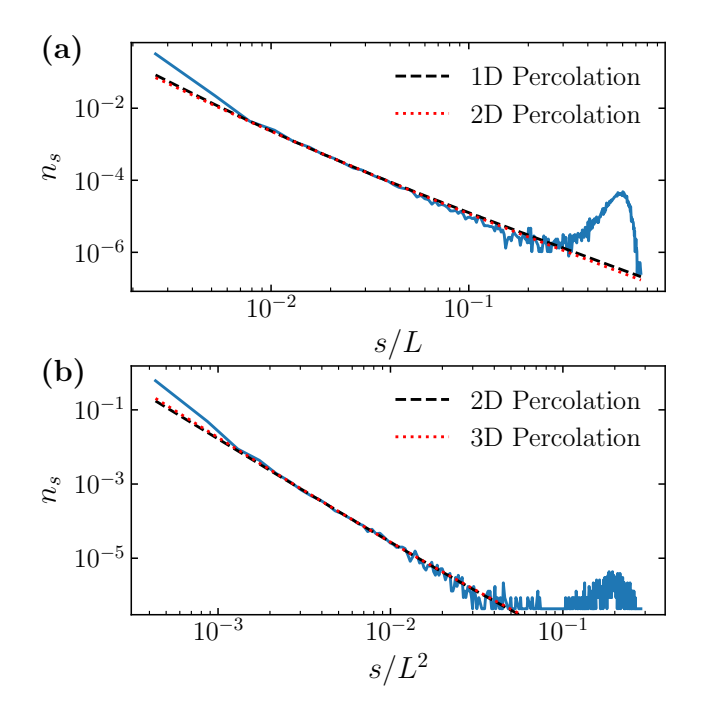


FIG. 12. Distribution function  $n_s$  of the entanglement cluster sizes s in the  $p=p_c$  steady state for (a) 1+1D and (b) 2+1D Clifford circuits, with system sizes L=348 and  $L^2=48^2$  respectively. For  $1 \ll s \ll L^d$ , the probability distribution follows a power-law distribution  $n_s \sim s^{-\tau}(c_0+c_1s^{-\Omega})$  with the leading-order correction to scaling controlled by the exponent  $\Omega$ . The dashed and dotted lines show fits using the exponents from d- and (d+1)-dimensional percolation respectively. The peak at large s corresponds to the percolating cluster of size  $\mathcal{O}(L^d)$  present for  $p \leq p_c$ .

d-dimensional percolation exponents.

Finally, in Fig. 12 we show the distribution  $n_s$  of all cluster sizes s, which at  $p = p_c$  and for  $1 \ll s \ll L^d$  follows a power-law  $n_s \sim s^{-\tau}(c_0 + c_1 s^{-\Omega} + \cdots)$ , with the leadingorder correction to scaling controlled by the exponent  $\Omega$ . A comment on this scaling form is necessary if we are to make a comparison with 1D percolation. As noted above, for 1D percolation the critical probability is  $p_c = 1$ . This has the consequence that, strictly at  $p = p_c$ , there is only a single cluster which covers the whole system,  $s_{\text{max}} = L$ , so for cluster sizes  $s < s_{\text{max}}$  the cluster number  $n_s =$ 0. Nonetheless, one can meaningfully define the Fisher exponent  $\tau$  by analyzing the behavior of  $n_s$  for  $p < p_c$ , where one finds  $\tau = 2$  for 1D percolation. However, a key difference between the 1+1D hybrid quantum circuits we study and 1D percolation is that for the quantum circuits,  $1 - p_c \approx 0.84$  is different from unity, so there is still randomness at the critical point, and thus we can observe a full distribution of cluster sizes. This provides justification for continuing to use the scaling form  $n_s \sim$  $s^{-\tau}(c_0 + c_1 s^{-\Omega} + \cdots)$  to describe the cluster distribution function in 1+1D hybrid circuits.

In this case, it is harder to distinguish the behavior of dand (d+1)-dimensional percolation, since the exponents

for the leading term,  $\tau_{1D}=2$ ,  $\tau_{2D}=187/91\approx 2.05$  [76] and  $\tau_{3D}\approx 2.19$  [74], are all quite similar in magnitude. Indeed both  $\tau_{1D}$  and  $\tau_{2D}$  provide a reasonable fit to our 1+1D data (see Fig. 12a), and both  $\tau_{2D}$  and  $\tau_{3D}$  provide a reasonable fit to our 2+1D data (see Fig. 12b). An independent statistical bootstrap analysis [83] gives the exponents  $\tau\approx 2.04$  and  $\Omega\approx 0.15$  in 1+1D, and  $\tau\approx 1.98$  and  $\Omega\approx 1.04$  in 2+1D. However, it is hard to call these values physically meaningful, since allowing for variation in the scaling correction exponent  $\Omega$  provides considerable freedom to optimize the quality of the fit. What is at least clear is that the Fisher exponent  $\tau$  is close to values predicted by percolation theory in low dimensions, since our fitted values are far from the mean-field value  $\tau=2.5$ .

We conclude this section by noting that the entanglement cluster distribution is qualitatively similar to the stabilizer length distribution (SLD) introduced by Li, Chen and Fisher in Ref. [24]. Indeed, both have a powerlaw tail, and a volume-law peak which disappears upon entering the area-law phase. Furthermore, at criticality the exponent  $\tau$  of the power-law tail is close to 2 in both cases. In 1+1D the SLD has the nice property that it can be used to calculate the entanglement entropy itself—for example, a power-law exponent of 2 gives rise to a subleading  $\log L$  contribution to the entanglement entropy. However, it is not clear how to generalize the SLD to higher dimensions in a way that preserves this ability to calculate the entanglement entropy from the analogous 'stabilizer volume distribution'. From the entanglement cluster distribution we analyze here, it is possible to calculate the entanglement entropy provided one makes certain simplifying assumptions about the fractal structure of the entanglement clusters, but we defer further analysis of this link to future work.

## VI. DISCUSSION

Although the connection between measurement-induced transitions in random quantum circuits and classical percolation has been well established in 1+1D, we have shown that this picture is more intricate than currently thought. Most notably, we uncovered a novel phenomenon of 'dimensional hybridity', where bulk critical exponents of (d+1)-dimensional hybrid quantum circuits are close to those of (d+1)-dimensional percolation, yet certain surface critical exponents may differ, and certain properties of the entanglement clusters in the steady state are governed by exponents from bulk d-dimensional percolation. We should note that critical exponent estimates should be treated with some amount of caution, especially for small system sizes, as conformal field theories with zero central charge (like those appearing in current theories of the 1+1D transition [30]) can have logarithmic corrections to scaling [84, 85], which could result in systematic errors. However, the fact that we can observe dimensional hybridity across many exponents and both in 1+1D (where large system sizes are available) and 2+1D circuits, provides

strong support for this phenomenon. We expect a similar picture to extend to higher dimensions and other circuit models—although the detailed entanglement structure of non-stabilizer states cannot be fully captured by a single graph state, entanglement clusters only require a notion of factorizability, which is also present in non-Clifford models. This would imply that dimensional hybridity is an important feature in the universal properties of measurement-induced transitions.

There are many open questions about the nature and origin of dimensional hybridity. For example, the connection to lower-dimensional percolation is not obvious, given the potentially high-dimensional nature of the entanglement graphs due to non-local entanglement. It may be possible that these non-local connections can be mapped into local connections in a spacetime bulk, given that the entanglement is ultimately generated by local unitaries at some point in the past. To understand this it seems important to formulate a well-defined notion of spacetime connectivity applicable to these Clifford circuits. Such a picture is available for the Hartley entropy transition in Haar-random circuits [22], where the bulk transition directly maps on to (d+1)-dimensional percolation. If this were approximately the correct picture for the entanglement clusters we analyze here, then naively one might expect their critical properties to be controlled by surface exponents of (d+1)-dimensional percolation. The fact that we instead see bulk d-dimensional percolation exponents therefore suggests this picture cannot be correct in this context. This may be a consequence of the fact that we are using Clifford gates, not Haar-random gates, but also may be because we are looking at a slightly different notion of connectivity with the graph state clusters compared to the spacetime circuit picture of the Haar-Hartley transition. If one were able to develop an appropriate spacetime picture which captures the evolution of the graph state connectivity, then one would think that we would be seeing the surface exponents of that model. Understanding why those surface exponents look so close to bulk d-dimensional percolation exponents is an important task for future work.

Another possibility is that the structure of entanglement clusters can be embedded in lower dimensions, and that the corresponding graph states at the critical point are locally embeddable. Indeed, our results in 2+1D show relatively low connectivity present in the graphs and a large number of planar subgraphs at  $p=p_c$  ( $\sim 80\%$  weight of the entire graph at large system sizes). In general, it is likely that the final-time boundary has a role in the phenomenon of dimensional hybridity, as it is seemingly the only important lower-dimensional surface of the system.

The role of randomness in measurement-induced transitions is currently an open question. For example, disorder is important in the percolation transition in d>1 for its role in generating critical fluctuations of cluster sizes. However, although measurement-induced transitions were initially studied in random circuits, they have also been

observed when various degrees of randomness have been removed [24]. The fact that we observe 1D percolation exponents in 1+1D hybrid circuits brings an interesting perspective to this problem. For 1D percolation the critical probability is  $p_c=1$ , so there is no randomness at the critical point. On the other hand, we observe 1D percolation exponents in our 1+1D hybrid circuit with a critical probability of  $p_c\approx 0.16$ , where there is still significant randomness present at criticality.

We have also shown the coincidence of the purification transition and the entanglement transition in 2+1D. This may at first be surprising, given that the entanglement transition concerns spatial correlations between equal-time wavefunctions, while the purification transition concerns correlations in time of a non-local quantity. The results in this paper indicate that these two transitions may coincide in all dimensions. One possible explanation for this could be the conjecture of Ref. [31] that the nonunitary nature of the dynamics results in the real time coordinate in d spatial dimensions acting as imaginary time in the corresponding (d+1)-dimensional statistical mechanical model. In this sense space and time may become symmetric, so the coincidence of the entanglement transition and the purification transition would be less surprising. The coincidence of these transitions and our entanglement cluster analysis also suggest a way to investigate connections with quantum error-correction—the emergence of the critical entanglement cluster can be seen as the germination of the quantum error-correcting code that characterizes the stability of the volume-law phase.

Moving into higher dimensions raises several ques-

tions. One interesting direction is that of 'measurementprotected order' [33, 34], analogous to the 'localizationprotected order' afforded by many-body localization (MBL) [86, 87]. It is tempting to view the area-law side of the measurement-induced transition as a 'trivial' phase, but recent work has demonstrated that there can be stable symmetry-protected topological (SPT) order in the area-law phase, motivated by comparisons with the arealaw ground states of gapped Hamiltonians. However, it is only in dimensions  $d \geq 2$  that true topological order can exist [88], so it would be interesting to see if nontrivial topological order could be realized in the steady states of 2+1D hybrid quantum circuits. There is also the question of which types of order can be stabilized by measurements. There are significant constraints on possible phases stabilized by MBL: non-Abelian symmetries are forbidden [89], for example, as well as chiral order [90]. It is also possible that true MBL does not exist in d > 1 [8]. It is an important topic for future research to determine which restrictions, if any, are applicable to measurementprotected order. This may allow for considerably more freedom in the more general paradigm of understanding and classifying non-equilibrium phases of matter.

#### ACKNOWLEDGMENTS

We thank Brian Skinner, Matthew Fisher, Michael Gullans and David Huse for helpful discussions. A.P. and M.S. were funded by the European Research Council (ERC) under the European Union's Horizon 2020 research and innovation programme (grant agreement No. 853368). O.L. was supported by the Engineering and Physical Sciences Research Council [grant number EP/L015242/1].

- D. M. Basko, I. L. Aleiner, and B. L. Altshuler, Metal-insulator transition in a weakly interacting manyelectron system with localized single-particle states, Ann. Phys. (N. Y.) 321, 1126 (2006).
- [2] I. V. Gornyi, A. D. Mirlin, and D. G. Polyakov, Interacting electrons in disordered wires: Anderson localization and low-t transport, Phys. Rev. Lett. 95, 206603 (2005).
- [3] A. Pal and D. A. Huse, Many-body localization phase transition, Phys. Rev. B 82, 174411 (2010).
- [4] R. Nandkishore and D. A. Huse, Many-Body Localization and Thermalization in Quantum Statistical Mechanics, Annu. Rev. Condens. Matter Phys. 6, 15 (2015).
- [5] D. A. Abanin, E. Altman, I. Bloch, and M. Serbyn, Colloquium: Many-body localization, thermalization, and entanglement, Rev. Mod. Phys. 91, 021001 (2019).
- [6] S. A. Parameswaran and R. Vasseur, Many-body localization, symmetry and topology, Rep. Prog. Phys. 81, 082501 (2018).
- [7] A. Chandran, A. Pal, C. R. Laumann, and A. Scardicchio, Many-body localization beyond eigenstates in all dimensions, Phys. Rev. B 94, 144203 (2016).
- [8] W. De Roeck and F. Huveneers, Stability and instability towards delocalization in many-body localization systems, Phys. Rev. B 95, 155129 (2017).

- [9] T. B. Wahl, A. Pal, and S. H. Simon, Signatures of the many-body localized regime in two dimensions, Nature Physics 15, 164 (2019).
- [10] S. Gopalakrishnan and D. A. Huse, Instability of many-body localized systems as a phase transition in a non-standard thermodynamic limit, Phys. Rev. B 99, 134305 (2019).
- [11] E. V. H. Doggen, I. V. Gornyi, A. D. Mirlin, and D. G. Polyakov, Slow many-body delocalization beyond one dimension, Phys. Rev. Lett. 125, 155701 (2020).
- [12] A. Nahum, J. Ruhman, S. Vijay, and J. Haah, Quantum entanglement growth under random unitary dynamics, Phys. Rev. X 7, 031016 (2017).
- [13] A. Chan, A. De Luca, and J. T. Chalker, Solution of a minimal model for many-body quantum chaos, Phys. Rev. X 8, 041019 (2018).
- [14] B. Bertini, P. Kos, and T. c. v. Prosen, Entanglement spreading in a minimal model of maximal many-body quantum chaos, Phys. Rev. X 9, 021033 (2019).
- [15] T. Farshi, D. Toniolo, C. E. González-Guillén, Á. M. Alhambra, and L. Masanes, Time-periodic dynamics generates pseudo-random unitaries, (2020), arXiv:2007.03339.
- [16] J. Preskill, Quantum Computing in the NISQ era and beyond, Quantum 2, 79 (2018).

- [17] F. Arute, K. Arya, R. Babbush, D. Bacon, J. C. Bardin, R. Barends, R. Biswas, S. Boixo, F. G. Brandao, D. A. Buell, et al., Quantum supremacy using a programmable superconducting processor, Nature 574, 505 (2019).
- [18] K. A. Landsman, C. Figgatt, T. Schuster, N. M. Linke, B. Yoshida, N. Y. Yao, and C. Monroe, Verified quantum information scrambling, Nature 567, 61 (2019).
- [19] L. D'Alessio, Y. Kafri, A. Polkovnikov, and M. Rigol, From quantum chaos and eigenstate thermalization to statistical mechanics and thermodynamics, Adv. Phys. 65, 239 (2016).
- [20] Y. Li, X. Chen, and M. P. A. Fisher, Quantum Zeno effect and the many-body entanglement transition, Phys. Rev. B 98, 205136 (2018).
- [21] A. Chan, R. M. Nandkishore, M. Pretko, and G. Smith, Unitary-projective entanglement dynamics, Phys. Rev. B 99, 224307 (2019).
- [22] B. Skinner, J. Ruhman, and A. Nahum, Measurement-Induced Phase Transitions in the Dynamics of Entanglement, Phys. Rev. X 9, 031009 (2019).
- [23] M. Szyniszewski, A. Romito, and H. Schomerus, Entanglement transition from variable-strength weak measurements, Phys. Rev. B 100, 064204 (2019).
- [24] Y. Li, X. Chen, and M. P. A. Fisher, Measurement-driven entanglement transition in hybrid quantum circuits, Phys. Rev. B 100, 134306 (2019).
- [25] J. Napp, R. L. La Placa, A. M. Dalzell, F. G. S. L. Brandao, and A. W. Harrow, Efficient classical simulation of random shallow 2D quantum circuits, arXiv:2001.00021 (2019).
- [26] A. Zabalo, M. J. Gullans, J. H. Wilson, S. Gopalakrishnan, D. A. Huse, and J. H. Pixley, Critical properties of the measurement-induced transition in random quantum circuits, Phys. Rev. B 101, 060301 (2020).
- [27] R. Fan, S. Vijay, A. Vishwanath, and Y.-Z. You, Self-Organized Error Correction in Random Unitary Circuits with Measurement, arXiv:2002.12385 (2020).
- [28] M. J. Gullans and D. A. Huse, Dynamical Purification Phase Transition Induced by Quantum Measurements, Physical Review X 10, 041020 (2020).
- [29] Y. Bao, S. Choi, and E. Altman, Theory of the phase transition in random unitary circuits with measurements, Phys. Rev. B 101, 104301 (2020).
- [30] C.-M. Jian, Y.-Z. You, R. Vasseur, and A. W. W. Ludwig, Measurement-induced criticality in random quantum circuits, Phys. Rev. B 101, 104302 (2020).
- [31] Y. Li, X. Chen, A. W. W. Ludwig, and M. P. A. Fisher, Conformal invariance and quantum non-locality in hybrid quantum circuits, arXiv:2003.12721 (2020).
- [32] O. Shtanko, Y. A. Kharkov, L. P. García-Pintos, and A. V. Gorshkov, Classical Models of Entanglement in Monitored Random Circuits, arXiv:2004.06736 (2020).
- [33] A. Lavasani, Y. Alavirad, and M. Barkeshli, Measurementinduced topological entanglement transitions in symmetric random quantum circuits, arXiv:2004.07243 (2020).
- [34] S. Sang and T. H. Hsieh, Measurement Protected Quantum Phases, arXiv:2004.09509 (2020).
- [35] M. Szyniszewski, A. Romito, and H. Schomerus, Universality of entanglement transitions from stroboscopic to continuous measurements, arXiv:2005.01863 (2020).
- [36] L. Zhang, J. A. Reyes, S. Kourtis, C. Chamon, E. R. Mucciolo, and A. E. Ruckenstein, Nonuniversal entanglement level statistics in projection-driven quantum circuits, Phys. Rev. B 101, 235104 (2020).

- [37] S. Choi, Y. Bao, X.-L. Qi, and E. Altman, Quantum Error Correction in Scrambling Dynamics and Measurement-Induced Phase Transition, Phys. Rev. Lett. 125, 030505 (2020).
- [38] X. Turkeshi, R. Fazio, and M. Dalmonte, Measurementinduced criticality in (2+1)-dimensional hybrid quantum circuits, Phys. Rev. B 102, 014315 (2020).
- [39] M. J. Gullans and D. A. Huse, Scalable Probes of Measurement-Induced Criticality, Phys. Rev. Lett. 125, 070606 (2020).
- [40] A. Nahum, S. Roy, B. Skinner, and J. Ruhman, Measurement and entanglement phase transitions in all-to-all quantum circuits, on quantum trees, and in Landau-Ginsburg theory, arXiv:2009.11311 (2020).
- [41] X. Cao, A. Tilloy, and A. De Luca, Entanglement in a fermion chain under continuous monitoring, SciPost Physics 7, 024 (2019).
- [42] Q. Tang and W. Zhu, Measurement-induced phase transition: A case study in the nonintegrable model by densitymatrix renormalization group calculations, Phys. Rev. Research 2, 013022 (2020).
- [43] S. Goto and I. Danshita, Measurement-induced transitions of the entanglement scaling law in ultracold gases with controllable dissipation, Phys. Rev. A 102, 033316 (2020).
- [44] O. Alberton, M. Buchhold, and S. Diehl, Trajectory dependent entanglement transition in a free fermion chain – from extended criticality to area law, arXiv:2005.09722 (2020).
- [45] O. Lunt and A. Pal, Measurement-induced entanglement transitions in many-body localized systems, Phys. Rev. Research 2, 043072 (2020).
- [46] N. Lang and H. P. Büchler, Entanglement transition in the projective transverse field Ising model, Phys. Rev. B 102, 094204 (2020).
- [47] X. Chen, Y. Li, M. P. A. Fisher, and A. Lucas, Emergent conformal symmetry in nonunitary random dynamics of free fermions, Phys. Rev. Research 2, 033017 (2020).
- [48] C. Liu, P. Zhang, and X. Chen, Non-unitary dynamics of Sachdev-Ye-Kitaev chain, arXiv:2008.11955 (2020).
- [49] Y. Fuji and Y. Ashida, Measurement-induced quantum criticality under continuous monitoring, Phys. Rev. B 102, 054302 (2020).
- [50] M. Ippoliti, M. J. Gullans, S. Gopalakrishnan, D. A. Huse, and V. Khemani, Entanglement phase transitions in measurement-only dynamics, arXiv:2004.09560 (2020).
- [51] M. Van Regemortel, Z.-P. Cian, A. Seif, H. Dehghani, and M. Hafezi, Entanglement entropy scaling transition under competing monitoring protocols, arXiv:2008.08619 (2020).
- [52] D. Aharonov, Quantum to classical phase transition in noisy quantum computers, Phys. Rev. A 62, 062311 (2000).
- [53] S. Vijay, Measurement-Driven Phase Transition within a Volume-Law Entangled Phase, arXiv:2005.03052 (2020).
- [54] A. Nahum and B. Skinner, Entanglement and dynamics of diffusion-annihilation processes with Majorana defects, Phys. Rev. Research 2, 023288 (2020).
- [55] Y. Li and M. P. A. Fisher, Statistical Mechanics of Quantum Error-Correcting Codes, arXiv:2007.03822 (2020).
- [56] D. Rossini and E. Vicari, Measurement-induced dynamics of many-body systems at quantum criticality, Phys. Rev. B 102, 035119 (2020).
- [57] M. J. Gullans, S. Krastanov, D. A. Huse, L. Jiang, and S. T. Flammia, Quantum coding with low-depth random

- circuits, arXiv:2010.09775 (2020).
- [58] L. Fidkowski, J. Haah, and M. B. Hastings, How Dynamical Quantum Memories Forget, arXiv:2008.10611 (2020).
- [59] T. Maimbourg, D. M. Basko, M. Holzmann, and A. Rosso, Bath-induced Zeno localization in driven many-body quantum systems, arXiv:2009.11784 (2020).
- [60] J. Iaconis, A. Lucas, and X. Chen, Measurementinduced phase transitions in quantum automaton circuits, arXiv:2010.02196 (2020).
- [61] M. Ippoliti and V. Khemani, Postselection-free entanglement dynamics via spacetime duality, (2020), arXiv:2010.15840.
- [62] A. Lavasani, Y. Alavirad, and M. Barkeshli, Topological order and criticality in (2+1)D monitored random quantum circuits, (2020), arXiv:2011.06595.
- [63] S. Sang, Y. Li, T. Zhou, X. Chen, T. H. Hsieh, and M. P. A. Fisher, Entanglement Negativity at Measurement-Induced Criticality, (2020), arXiv:2012.00031.
- [64] B. Shi, X. Dai, and Y.-M. Lu, Entanglement negativity at the critical point of measurement-driven transition, (2020), arXiv:2012.00040.
- [65] S. Gopalakrishnan and M. J. Gullans, Entanglement and purification transitions in non-Hermitian quantum mechanics, (2020), arXiv:2012.01435.
- [66] A. Nahum, J. Ruhman, S. Vijay, and J. Haah, Quantum Entanglement Growth under Random Unitary Dynamics, Phys. Rev. X 7, 031016 (2017).
- [67] S. Anders and H. J. Briegel, Fast simulation of stabilizer circuits using a graph-state representation, Phys. Rev. A 73, 022334 (2006).
- [68] P. Calabrese and J. Cardy, Entanglement entropy and quantum field theory, J. Stat. Mech: Theory Exp. 2004, P06002 (2004).
- [69] E. Fradkin and J. E. Moore, Entanglement Entropy of 2D Conformal Quantum Critical Points: Hearing the Shape of a Quantum Drum, Phys. Rev. Lett. 97, 050404 (2006).
- [70] M. Hein, J. Eisert, and H. J. Briegel, Multiparty entanglement in graph states, Phys. Rev. A 69, 062311 (2004).
- [71] D. Fattal, T. S. Cubitt, Y. Yamamoto, S. Bravyi, and I. L. Chuang, Entanglement in the stabilizer formalism, (2004), arXiv:quant-ph/0406168.
- [72] N. Kawashima and N. Ito, Critical Behavior of the Three-Dimensional ±J Model in a Magnetic Field, J. Phys. Soc. Jpn. 62, 435 (1993).
- [73] Z. Koza and J. Poła, From discrete to continuous percolation in dimensions 3 to 7, J. Stat. Mech: Theory Exp. 2016, 103206 (2016).
- [74] X. Xu, J. Wang, J.-P. Lv, and Y. Deng, Simultaneous analysis of three-dimensional percolation models, Front. Phys. 9, 113 (2014).
- [75] A. S. Skal and B. I. Shklovskii, Topology of an infinite cluster in the theory of percolation and its relationship to the theory of hopping conduction, Sov. Phys. Semicond. 8, 1029 (1975), English version; original publication in Fiz. Tekh. Poluprov. 8, 1586 (1974).
- [76] D. Stauffer and A. Aharony, *Introduction To Percolation Theory: Second Edition* (Taylor & Francis, 2018).
- [77] M. P. Gelfand and M. E. Fisher, Finite-size effects in fluid interfaces, Physica A 166, 1 (1990).
- [78] M. M. Wolf, F. Verstraete, M. B. Hastings, and J. I. Cirac, Area Laws in Quantum Systems: Mutual Information and Correlations, Phys. Rev. Lett. 100, 070502 (2008).
- [79] J. A. Gracey, Four loop renormalization of  $\phi^3$  theory in six dimensions, Phys. Rev. D **92**, 025012 (2015).

- [80] T. Cormen, C. E. Leiserson, R. L. Rivest, and C. Stein, Introduction to Algorithms. 3rd ed. (The MIT Press, 2009).
- [81] Y. Deng and H. W. J. Blöte, Surface critical phenomena in three-dimensional percolation, Phys. Rev. E 71, 016117 (2005).
- [82] C. Vanderzande, Surface fractal dimension of twodimensional percolation, Journal of Physics A: Mathematical and General 21, 833 (1988).
- [83] B. Efron and R. J. Tibshirani, An Introduction to the Bootstrap (Chapman and Hall/CRC, 1994).
- [84] V. Gurarie and A. W. W. Ludwig, Conformal algebras of two-dimensional disordered systems, J. Phys. A: Math. Gen. 35, L377 (2002).
- [85] J. Cardy, Logarithmic conformal field theories as limits of ordinary CFTs and some physical applications, J. Phys. A: Math. Theor. 46, 494001 (2013).
- [86] D. A. Huse, R. Nandkishore, V. Oganesyan, A. Pal, and S. L. Sondhi, Localization-protected quantum order, Phys. Rev. B 88, 014206 (2013).
- [87] B. Bauer and C. Nayak, Area laws in a many-body localized state and its implications for topological order, J. Stat. Mech: Theory Exp. 2013, P09005 (2013).
- [88] N. Schuch, D. Pérez-García, and I. Cirac, Classifying quantum phases using matrix product states and projected entangled pair states, Phys. Rev. B 84, 165139 (2011).
- [89] A. C. Potter and R. Vasseur, Symmetry constraints on many-body localization, Phys. Rev. B 94, 224206 (2016).
- 90] A. C. Potter and A. Vishwanath, Protection of topological order by symmetry and many-body localization, arXiv:1506.00592 (2015).

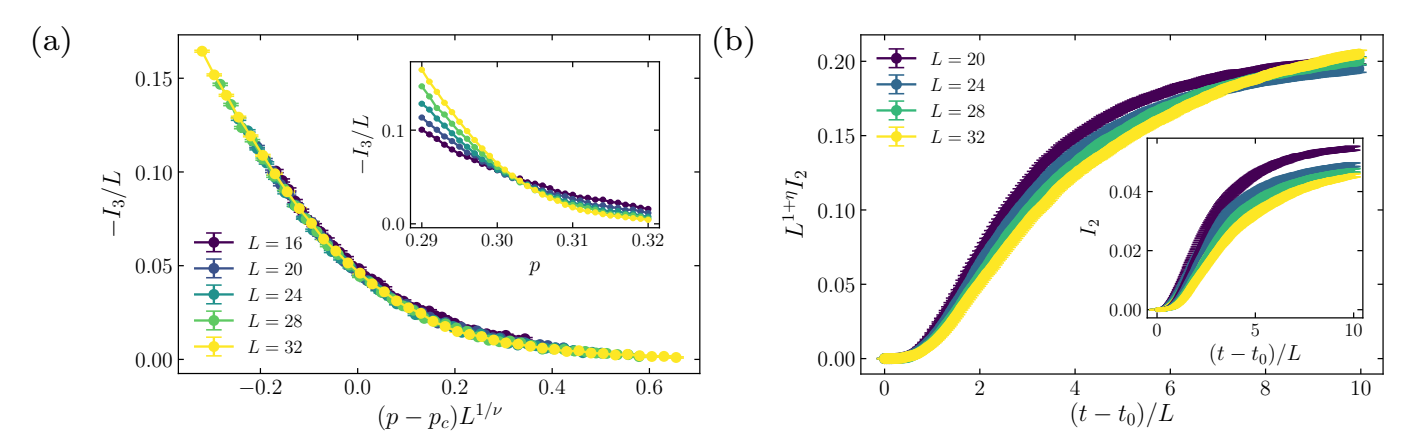


FIG. A1. (a) The steady-state values of  $I_3/L$  as a function of  $(p-p_c)L^{1/\nu}$ , where  $p_c \approx 0.303$  and  $\nu \approx 1.07$ . The inset shows the uncollapsed data. This dataset consists of 50,000 circuit realizations. (b) Analogous to Fig. 8a, except performed at the alternative critical point  $p_c \approx 0.303$  estimated from the data collapse of  $I_3/L$ . The main plot shows the 'optimal' collapse at  $\eta = -0.57$  as determined by minimizing the cost function in Appendix B, but this clearly does not produce a good data collapse.

## Appendix A: Alternative scaling forms for $I_3$

In this section we detail some evidence against the hypothesis that  $I_3 \sim \mathcal{O}(L)$  at  $p = p_c$ . Finite-size scaling of  $I_3/L$ results in the critical point  $p_c \approx 0.303$  with  $\nu \approx 1.07$  (see Fig. A1a). However, if we attempt to use this critical point to estimate other critical exponents from standard finite-size scaling arguments, we are unable to obtain a good data collapse, indicating the absence of scaling behavior. For example, to extract the anomalous scaling exponent  $\eta$ , we follow the procedure detailed in Section IV, where  $\eta$  is chosen to optimize the data collapse of the dynamics of the mutual information between two ancilla qubits. Whereas this was possible for the critical point  $p_c \approx 0.312$  obtained from finite-size scaling of  $I_3$  (see Fig. 8a), for the purported critical point  $p_c \approx 0.303$  from  $I_3/L$  scaling, there was not a value of  $\eta$  for which a good data collapse was possible (see Fig. A1b). Moreover, the data collapse in Fig. A1a is of visibly worse quality than the excellent collapse in Fig. 4. We also see in Section IV that the purification transition seems to coincide with the critical point  $p_c \approx 0.312$  from  $I_3$  scaling, with a dynamical critical exponent  $z \approx 1$  indicating the emergence of conformal symmetry. Given that these facts mirror the situation in 1+1D, this provides further aposteriori justification for the scaling  $I_3 \sim \mathcal{O}(1)$  at criticality.

## Appendix B: Details of the finite-size scaling

To perform the data collapses, we use a cost function  $\epsilon(p_c, \nu)$  which uses linear interpolation to find the parameters  $(p_c, \nu)$  which cause the data to best collapse on to a single curve [26, 72]. In more detail, given a set of parameters  $(p_c, \nu)$ , for each value of p and L we create an x-value  $x := (p - p_c)L^{1/\nu}$ , with a corresponding y-value y(p, L) and error d(p,L). We then sort the triples  $(x_i, y_i, d_i)$  according to their x-values, and evaluate the cost function

$$\epsilon(p_c, \nu) := \frac{1}{n-2} \sum_{i=2}^{n-1} w(x_i, y_i, d_i | x_{i-1}, y_{i-1}, d_{i-1}, x_{i+1}, y_{i+1}, d_{i+1}), \tag{B1}$$

where  $w(x_i, y_i, d_i | x_{i-1}, y_{i-1}, d_{i-1}, x_{i+1}, y_{i+1}, d_{i+1})$  is defined as

$$w := \left(\frac{y - \bar{y}}{\Delta(y - \bar{y})}\right)^2,\tag{B2}$$

$$\bar{y} := \frac{(x_{i+1} - x_i)y_{i-1} - (x_{i-1} - x_i)y_{i+1}}{x_{i+1} - x_{i-1}},$$
(B3)

$$\bar{y} := \frac{(x_{i+1} - x_i)y_{i-1} - (x_{i-1} - x_i)y_{i+1}}{x_{i+1} - x_{i-1}},$$

$$|\Delta(y - \bar{y})|^2 := d_i^2 + \left(\frac{x_{i+1} - x_i}{x_{i+1} - x_{i-1}}\right)^2 d_{i-1}^2 + \left(\frac{x_{i-1} - x_i}{x_{i+1} - x_{i-1}}\right)^2 d_{i+1}^2.$$
(B3)

The function w measures the deviation of a point from the line obtained by a linear interpolation of its nearest neighbours, weighted by the errors in each data point. Values of  $(p_c, \nu)$  for which  $\epsilon(p_c, \nu) \approx 1$  are considered optimal.

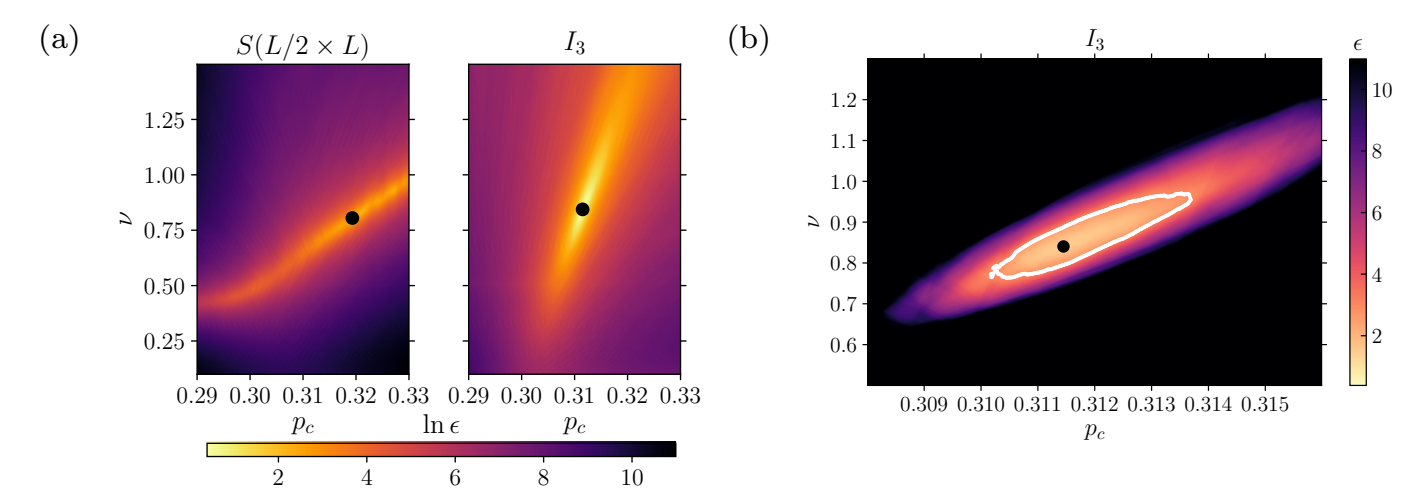


FIG. B2. (a) The logarithm of the cost function  $\epsilon$  measuring the quality of the data collapse for different values of  $p_c$  and  $\nu$ , compared between two possible indicators of the entanglement transition: the half-plane entanglement entropy S(L/2), and the tripartite information  $I_3$ . The black dots show the minimum of the cost function for each indicator. See the appendix for a definition of the cost function  $\epsilon$ . (b) A linear-scale close-up of the cost function for the  $I_3$  data collapse around the estimated critical point, which is indicated by the black dot. The white line indicates the boundary of the region for which the cost function is less than 2 times its minimum value; this is the region from which the error bars are calculated. At the estimated critical point the cost function attains the value  $\epsilon = 1.47$ , close to the optimal value  $\epsilon \approx 1$ .

As discussed in Section III, our finite-size scaling analysis yields the correlation length exponent  $\nu \approx 0.85(9)$ , which is significantly different to that observed in Ref. [38]. We attribute this to the fact that we extract  $\nu$  by a data collapse not of the half-plane entanglement, as in Ref. [38], but of the tripartite information, which coincides for different system sizes at the critical point and so provides a much more accurate estimator of the critical point. To further this point, we show in Fig. B2a a comparison of the cost function  $\epsilon(p_c,\nu)$  landscape in log scale between the half-plane entropy  $S(L/2 \times L)$  and the tripartite information  $I_3$ . The entropy cost function plot shows a clear 'ridge' region where  $\epsilon$  is roughly constant, spanning the whole range of values of  $p_c$  and with a large variation of  $\nu$  along the ridge (see also Fig. 2 in the Erratum of Ref. [38]). On the other hand, the  $I_3$  cost function plot is much more localized around the estimated critical parameters, reaching a smaller value of  $\epsilon$  than the entropy plot. This localization is less obvious viewed in log scale, but the log was necessary for a meaningful visual comparison of the cost function plots for the two indicators. Fig. B2b shows a linear-scale version of the cost function plot for  $I_3$ , which allows for a clearer visualization of the localization of the cost function minimum. The estimated critical point is indicated by the large black dot, while the surrounding white line gives the boundary of the region where the cost function is less than 2 times its minimum value, from which we calculate the error bars in  $p_c$  and  $\nu$ . Notice that at the estimated critical point, the cost function reaches a value  $\epsilon = 1.47$  close to 1, indicating a good-quality data collapse.

Furthermore, a comment on the used system sizes is necessary. One could argue that the 4 subsystems used to calculate  $I_3$  have the vertical dimension  $L_y \leq 8$ , which may be small enough to exhibit substantial finite-size effects, hindering our ability to properly locate the critical point. However,  $I_3$  in 1+1D circuits shows almost no finite-size drift at criticality already for systems of size  $L \geq 16$  [26] (subsystems of size  $\geq 4$ ). Using our data from Fig. 4, one can assess that the crossings of  $I_3$  exhibit no statistically significant drift above roughly  $L \geq 16$ , strongly implying little to no finite-size effects in  $I_3$  at criticality for the system sizes considered. We also note that the data collapse is of exceptional quality, again strongly ruling out any substantial finite-size drifts.

## Appendix C: Details of the entanglement clusters

In this section we detail some data regarding the effective dimensionality of the entanglement graphs we investigate in Section V, which describe the steady-states of (d+1)-dimensional hybrid quantum circuits. There we find that many of the properties of the clusters in these graphs are controlled by exponents from d-dimensional percolation, where we analyze the cases d=1 and d=2. This may be surprising, given that these entanglement graphs could potentially be very high-dimensional due to the presence of non-local entanglement. One hypothesis that might explain this is if the entanglement graphs remain d-dimensional close to criticality, and are only higher dimensional deep within the volume-law phase where there is a large build-up of non-local entanglement.

To investigate precisely how non-local this entanglement is, we investigated the typical distance of edges in the

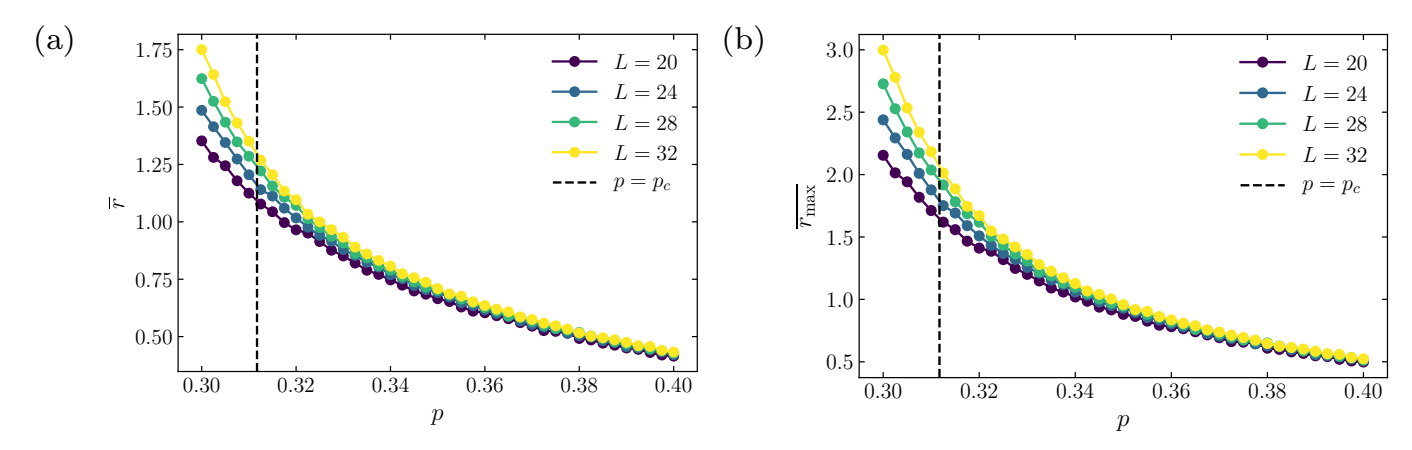


FIG. C3. (a) The mean edge distance  $\overline{r}$  of the steady-state entanglement graph, where the distance of an edge between two nodes is defined as the Manhattan distance between on the  $L \times L$  lattice. (b) The mean max edge distance  $\overline{r}_{max}$  of the steady-state entanglement graph. The maximum is taken for each vertex before doing the average.

entanglement graph describing the steady-state in 2+1D, where by 'distance' we mean the physical distance between the spins on the physical  $L \times L$  lattice. In Fig. C3a we show the mean edge distance  $\overline{r}$ , where the average is over all nodes and over circuit realizations. If a spin is not connected to any others in the entanglement graph, we record its edge distance as zero, which is why  $\overline{r}$  goes below one in the area-law phase. However, at criticality,  $\overline{r} > 1$ , and indeed seems to grow as a power-law with exponent  $\approx 1/4$ . We observe that power-law up to system size L=48, although we cannot rule out that it saturates to some finite value at larger system sizes. At any rate, the point is that  $\overline{r} > 1$ , so that at criticality the entanglement graph has connections beyond those of a simple two-dimensional square lattice. We also show in Fig. C3b the mean max edge distance  $\overline{r}_{max}$ , where we take the maximum edge distance for each node, before averaging over nodes and circuit realizations. This quantity grows as a power-law at criticality with an exponent  $\approx 0.35$ . However, it is again possible that this edge distance saturates to some finite value at larger system sizes than those accessible to us. This could imply that, although the entanglement graph is not two-dimensional at criticality, it might be quasi two-dimensional, in the sense that the mean edge distance is sufficiently small that a small extension of the graph into a third dimension might be sufficient to embed all of its edges.